POLITECNICO DI TORINO
Repository ISTITUZIONALE

Development and Validation of a Combustion Model for a High-Performance H2 Engine Considering Thermo-Diffusive Instability Effects

Original
Development and Validation of a Combustion Model for a High-Performance H2 Engine Considering Thermo-Diffusive Instability Effects / Rolando, L., Montanaro, G., Piano, A., Millo, F., Mortellaro, F., Tonelli, R.. - In: ENERGIES. - ISSN 1996-1073. - ELETTRONICO. - 19:18(2026). [10.3390/en19184250]

Availability:
This version is available at: 11583/3018044 since: 2026-11-17T15:28:47Z

Publisher:
Multidisciplinary Digital Publishing Institute (MDPI)

Published
DOI:10.3390/en19184250

Terms of use:

This article is made available under terms and conditions as specified in the corresponding bibliographic description in the repository

Publisher copyright

(Article begins on next page)

21 November 2026

energies

MDPI

Article

Development and Validation of a Combustion Model for a High-Performance H_2 Engine Considering Thermo-Diffusive Instability Effects

Luciano Rolando [1,*], Giancarlo Montanaro [1], Andrea Piano [1], Federico Millo [1], Fabio Mortellaro [2] and Roberto Tonelli [2]

[1] Energy Department, Politecnico di Torino, Corso Duca degli Abruzzi 24, 10129 Torino, Italy; giancarlo.montanaro@polito.it (G.M.); andrea.piano@polito.it (A.P.); federico.millo@polito.it (F.M.)
[2] Powertrain Simulation & Know-How, Ferrari S.p.A., Via Abetone Inferiore 4, 41053 Maranello, Italy; fabio.mortellaro@ferrari.com (F.M.); roberto.tonelli@ferrari.com (R.T.)
* Correspondence: luciano.rolando@polito.it; Tel.: +39-348-499-2145

Abstract

This study presents the development and validation of a predictive 0D/1D combustion model for a high-performance direct injection hydrogen spark-ignition engine, explicitly incorporating thermo-diffusive instability (TDI) effects through a physics-based formulation derived from linear flame stability theory and DNS-informed scaling laws. A laminar flame speed correlation obtained from detailed chemical kinetics is enhanced via an instability growth-rate model and embedded within an entrainment-based turbulent combustion framework, coupled with an Extended Zeldovich mechanism for NO_x prediction. The model is validated against experiments covering 2000–7500 rpm, loads up to 28 bar IMEP-H, and relative air-to-fuel ratio between 1.2 and 3.0. The results demonstrate that instability-aware modeling is essential for accurate ultra-lean combustion prediction, where conventional approaches severely underpredict burning rates. Across the full operating map, combustion phasing is predicted within ± 3 CAD and NO_x with an average error of 20%, enabling robust system-level simulation and virtual calibration of high-performance hydrogen engines.

Keywords: high-performance hydrogen engine; thermo-diffusive instability; instability-aware 1D combustion modeling; ultra-lean combustion; NO_x emissions prediction

Check for updates

Academic Editor: Maria Founti

Received: 20 July 2026
Revised: 31 August 2026
Accepted: 3 September 2026
Published: 8 September 2026

Copyright: © 2026 by the authors. Licensee MDPI, Basel, Switzerland. This article is an open access article distributed under the terms and conditions of the Creative Commons Attribution (CC BY) license.

1. Introduction

Hydrogen Internal Combustion Engines (H_2-ICEs) are currently being actively developed as a complementary propulsion solution in sectors where electrification alone remains challenging, including high-performance engine applications characterized by specific power levels of approximately 140 kW/L, as well as heavy-duty applications [1,2]. In high-performance engines, hydrogen enables rapid combustion and high specific power density due to its fast chemical kinetics and wide flammability limits, while in heavy-duty contexts, it allows stable ultra-lean operation and high thermal efficiency under high load [3,4]. Direct injection (DI) architectures are particularly relevant, as they mitigate volumetric efficiency penalties typical of premixed configurations and enable competitive power output together with dilution-based nitrogen oxide (NO_x) control [3].

However, hydrogen combustion presents significant modeling challenges arising from its distinct physicochemical properties, including high diffusivity, low ignition energy, and

an effective Lewis number lower than unity under lean conditions. These characteristics promote thermo-diffusive instability (TDI), leading to cellular flame structures and substantial enhancement of the effective burning velocity [5,6]. High-fidelity investigations using DNS and detailed CFD have demonstrated that instability-driven flame acceleration becomes dominant in ultra-lean hydrogen mixtures [6,7]. More recently, Scalambro et al. [8] provided a detailed analysis of thermo-diffusive instability mechanisms in hydrogen DI engines, quantitatively linking instability growth to combustion development under engine-relevant thermodynamic conditions.

While these mechanisms are well characterized in high-fidelity simulations, their integration into system engine models remains limited. In practical engine development, full operating maps—covering speed, load, and dilution sweeps—must be evaluated repeatedly for calibration and optimization purposes. This requires 0D/1D system-level models capable of resolving combustion phasing, burn duration, and emissions at reasonable computational cost. In this context, entrainment-based turbulent combustion models remain widely adopted [9,10]; however, most implementations either neglect thermo-diffusive effects or incorporate them through empirical adjustments without explicit physical grounding. Although recent phenomenological approaches have introduced instability-aware corrections in hydrogen PFI engines [11], validation under high-speed, high-load direct injection conditions—where turbulence–instability interactions are amplified—remains scarce.

Building upon fundamental instability analyses recently conducted for engine-relevant conditions [8] and phenomenological models proposed for PFI architectures [11], the primary novelty of the present work lies in the integration and extensive validation of a physics-based thermo-diffusive formulation [6,12,13] within a system-level, entrainment-based 0D/1D framework specifically tailored for a high-speed, high-load direct injection hydrogen engine.

The resulting instability-aware combustion model is validated against an extensive experimental dataset spanning 2000–7500 rpm, loads up to 28 bar Gross Indicated Mean Effective Pressure (IMEP-H), and relative A/F ratio from λ = 1.2 to 3.0. Particular emphasis is placed on quantifying the role of thermo-diffusive effects across lean operating conditions and assessing their impact on system-level predictive accuracy.

The manuscript is organized as follows: Section 2 describes the experimental setup and dataset; Section 3 details the modeling framework; Section 4 presents results and sensitivity analysis, followed by a dedicated discussion of the physical implications of instability-aware modeling; and Section 5 summarizes the main conclusions and perspectives.

2. Experimental Investigations

2.1. Tested Engine

The experimental investigation was conducted on a Single-Cylinder Engine (SCE) derived from a high-performance turbocharged V6 Gasoline Direct Injection (GDI) engine and adapted for hydrogen operation. The overall combustion system architecture was retained from the production engine; however, selected components, including the piston, were redesigned to withstand the higher in-cylinder pressures and associated mechanical loads. Hydrogen is supplied by a dedicated injector centrally mounted within the combustion chamber, while the spark plug is positioned on the exhaust side (see Table 1).

Table 1. Single-cylinder engine specifications.

Displacement	cc	498.7
Stroke	mm	82
Bore	mm	88
Compression ratio	-	10.5:1
Number of valves	-	4
H2 injector	-	Direct—Central mounted
H2 pressure	bar	5–40
Ignition	-	Exhaust side spark plug
Speed range	RPM	2000–7500
Max IMEP-H	bar	32 [14]

The fuel was supplied from a high-pressure external storage system and delivered through a pressure regulator, enabling injection pressures between 5 and 40 bar, and through a Coriolis mass flow sensor (Endress + Hauser Promass A, maximum capacity 100 kg/h). Furthermore, the injection temperature was actively controlled during the test thanks to the use of a dedicated heat exchanger.

From the periphery perspective, the intake system is composed of two entrances for naturally aspirated and boosted conditions, respectively, a heat exchanger to control the air temperature, a Hot Film Anemometer (HFM) to measure the mass flow rate, and a plenum to damp pressure oscillations. Downstream, a Helmholtz resonator is used to mimic the pressure waves of the multicylinder engine (see Figure 1).

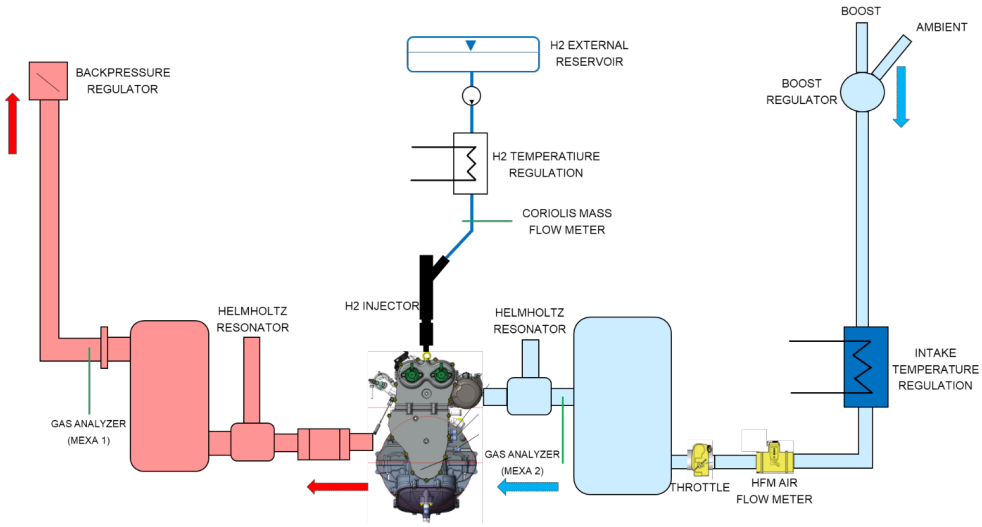


Figure 1. Scheme of the experimental setup with focus on temperature and pressure regulators on different parts of the layout.

In-cylinder pressure was measured using a piezoelectric pressure transducer installed between the intake and exhaust valves, while runner pressures were monitored via piezoresistive sensors. On the exhaust side, a second resonator is positioned upstream of the plenum, and at its outlet a V&F HSense mass spectrometer was used, in combination with a Bosch LSU5.2 lambda sensor, to measure the pollutant species concentration and the air-to-fuel (A/F) ratio [15]. Finally, a pressure regulator is used to set different backpressure levels at the engine outlet.

All tests were performed under steady-state conditions across a wide range of speeds and loads. For each operating point, in-cylinder pressure traces were recorded over 200 consecutive cycles, while test bench signals were averaged over a 30 s acquisition window to ensure stable conditions.

2.2. Experimental Dataset

A comprehensive experimental campaign was performed to cover the entire range of engine operating conditions.

Figure 2 summarizes the complete dataset in terms of Gross Indicated Mean Effective Pressure as a function of the relative A/F ratio (λ). Data points are color-coded according to the rotational speed, while marker shape indicates injection strategy (early or late SOI). Red diamonds identify the operating points used for model calibration. Moreover, as reported in Table 2, the data points could be divided into Rated Power and Part Load regions, respectively. The former includes 79 steady-state points at engine speeds between 6000 and 7500 rpm, with IMEP-H values exceeding 15 bar and reaching up to 28 bar (limited by the onset of pre-ignition). The air–fuel ratio ranges from λ = 1.2 to λ = 3.0. Thermally severe boundary conditions were imposed: intake air temperature was fixed at 65 °C, hydrogen temperature at 50 °C, and exhaust backpressure was controlled to reproduce multicylinder operating conditions. The Center of Combustion (CoC) was adjusted via spark timing to achieve Maximum Brake Torque (MBT) operation (approximately 8° aTDCf) or limited by abnormal combustion.

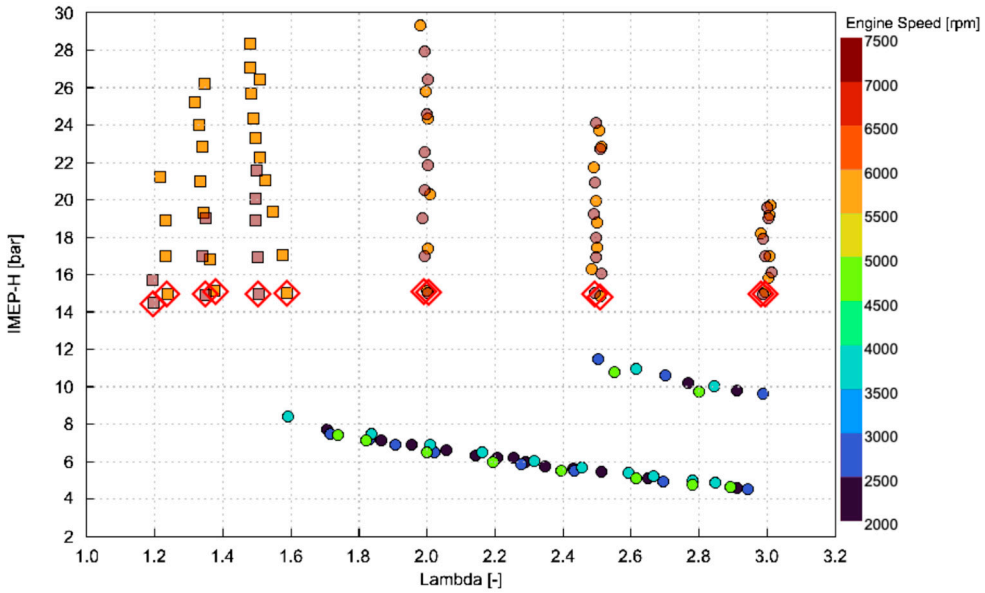


Figure 2. Experimental dataset in terms of IMEP-H as a function of lambda. The color of the indicator represents the engine rotation speed, while its shape represents the injection phasing: square for late injection while circle for early injection (early if SOI > 165 deg bTDCf). Red diamonds identify the calibration points.

Table 2. Experimental dataset characteristics.

	Rated Power	**Part Load**
Engine speed	6000–7500	2000–3000–4000–5000
IMEP-H	≥15 bar	<15 bar
Lambda	From 1.2 to 3	From 1.6 to 3
Intake air temperature	65 °C	T_{AMB}
H2 injection temperature	50 °C	25 °C
Backpressure	Multicylinder levels in similar conditions	P_{AMB}

The second region is representative of real-driving scenarios, and it investigates part-load operation between 2000–5000 rpm and 4–13 bar IMEP-H. The air–fuel ratio spans λ = 1.6–3.0 while intake and hydrogen temperatures were maintained near ambient conditions, and no exhaust backpressure was imposed. Injection timing and spark advance

(set at MBT) were kept constant to isolate the influence of speed and air–fuel ratio on combustion development and emissions.

3. Modeling Approach

Accurate prediction of engine performance and NO_x emissions in hydrogen-fueled spark-ignition engines requires a combustion formulation capable of capturing both turbulence–chemistry interactions and the specific instability mechanisms typical of lean hydrogen flames. Therefore, a comprehensive simulation framework was developed in the commercial software GT-SUITE for the investigated DI hydrogen engine. This platform integrates a physics-based, entrainment turbulent combustion model with a customized laminar flame speed correlation. The latter is derived from detailed chemical kinetics and explicitly includes a correction for TDI effects. To predict emissions, an Extended Zeldovich NO_x sub-model was coupled to the framework.

3.1. Turbulent Combustion Modeling

The combustion process is described using the SITurb model [9,10], a phenomenological, entrainment-based formulation originally derived from the work of Blizard and Keck [9]. This model adopts a two-zone framework where the turbulent flame front is treated as a spherically expanding flame brush that separates the unburned and burned gases. The combustion process is decoupled into two distinct physical mechanisms: the entrainment of the unburned mixture into the turbulent flame brush, and the subsequent burn-up of the entrained mass, which is governed by laminar chemistry. The entrainment rate is expressed as:

$$\frac{dM_e}{dt} = \rho_u A_f (S_T + S_L) \tag{1}$$

where M_e is the entrained mass, ρ_u the unburned gas density, A_f the flame surface area, S_L the laminar flame speed, and S_T the turbulent flame speed. The burn-up rate of the entrained mass is:

$$\frac{dM_b}{dt} = \frac{M_e - M_b}{\tau} \tag{2}$$

where M_b is the burned mass, with the characteristic time scale τ:

$$\tau = \frac{\lambda_T}{S_L} = C_{TLS} \frac{L_i}{\sqrt{Re_t}} \frac{1}{S_L} \tag{3}$$

where λ_T is the Taylor microscale, L_i the integral length scale, Re_t the turbulent Reynolds number, and C_{TLS} a calibration coefficient controlling the flame brush thickness. The turbulent flame speed is given by:

$$S_T = C_{TFS} u' \left(1 - \frac{1}{1 + C_{FKG} \left(\frac{R_f}{L_i} \right)^2} \right) \tag{4}$$

where u' is turbulent intensity and R_f the flame radius. The coefficients C_{TFS} and C_{FKG} are calibration parameters, the latter governing the early flame kernel growth.

The turbulence-related quantities required by the SITurb model were provided by the phenomenological K-k-ϵ turbulence model available in GT-SUITE [16]. This turbulence model was calibrated against 3D-CFD cold-flow simulations for a representative set of operating points, ensuring consistency in the evolution of the Turbulent Kinetic Energy (TKE) and the integral length scale. Crucially, the model also captures the turbulence variations induced by the direct injection of hydrogen. Within this formulation, the laminar flame speed term S_L plays a central role, directly influencing both the entrainment and

burn-up time scales. Therefore, an accurate representation of laminar flame speed is critical for reliable hydrogen combustion modeling.

3.2. Hydrogen Laminar Flame Speed Modeling

The default hydrogen laminar flame speed model embedded in GT-SUITE relies on a neural network trained over a highly extended parameter space [17]. While this data-driven approach provides broad coverage suitable for a wide spectrum of conventional engine architectures [18], the extreme thermodynamic conditions characteristic of the high-performance application investigated in this study require a specific calibration.

To achieve higher predictive accuracy for this specific engine architecture, the default model was replaced with a custom, tailored correlation. This was derived from detailed 1D planar premixed flame simulations conducted using Cantera 3.0 [19].

The simulations employed the Konnov chemical kinetic mechanism [20], which consists of 5 elements, 15 species, and 76 elementary reactions. This mechanism was selected because it offers an optimal balance between computational tractability and precision. Furthermore, as demonstrated by Liu et al. [21] in a recent systematic evaluation of multiple kinetic schemes, the Konnov mechanism provides high predictive accuracy specifically under lean and high-pressure conditions, yielding an average error below 9.6% against experimental data. This robust performance justifies its selection as a reliable chemical baseline for the subsequent instability-aware scaling.

To ensure strict thermodynamic consistency with the experimental data, the parameter space for the new correlation was tailored to the operating envelope of the tested engine:

- Pressure: 5–250 bar
- Temperature: 550–1150 K
- Equivalence ratio: ϕ = 0.2–1.8

By restricting the formulation to these engine-relevant boundaries, the customized correlation provides superior fidelity within the specific conditions of this high-performance setup. Currently, the dependence on the residual gas fraction is not explicitly included and remains a potential area for future improvement. However, it should be noted that under the ultra-lean conditions investigated in this study, excess air acts as the primary source of mixture dilution. As a result, the thermodynamic and kinetic impacts of internal residuals can be reasonably considered a secondary effect compared to the primary influence of pressure, temperature, and equivalence ratio, providing an acceptable approximation for the current scope of the model.

3.3. Thermo-Diffusive Instability Calculation

While the laminar flame speed correlation provides a baseline for stable planar flames, lean hydrogen mixtures are characterized by effective Lewis numbers below unity (Le < 1), leading to thermo-diffusive instability. This phenomenon induces flame front wrinkling and cellular structures even under laminar conditions that significantly enhance the effective burning velocity [5,6].

The instability analysis follows the linear stability framework originally introduced by Landau [12] and extended by Matalon et al. [13] to account for variable transport properties and diffusive-thermal effects. The instability parameter, defined as the ratio between the cellular and planar laminar flame speeds (see Equation (5)), is evaluated through DNS-informed scaling relations proposed by Howarth et al. [6]:

$$\begin{cases} \frac{s_M}{s_L} = exp(0.08\omega_2), \; if \; P < \Pi_c \\ \frac{s_M}{s_L} = 1 + 0.47\omega_2, if \; P \geq \Pi_c \end{cases} \quad (5)$$

where P is the instantaneous in-cylinder pressure, Π_c denotes a critical pressure threshold separating two instability regimes, and ω_2 captures the thermo-diffusive contributions, which depend on the effective Lewis number, on the Zeldovich number, and on the Prandtl number (see Howarth et al. [6] for a detailed derivation).

The introduction of Π_c (see Equation (6)) is not purely empirical, but it reflects the well-documented pressure sensitivity of thermo-diffusive instability growth. At lower pressures, preferential diffusion effects are dominant, the flame is thicker, and cellular structures develop rapidly, causing an exponential amplification of the instability. As pressure increases, the flame thickness decreases, and diffusive transport effects are damped by hydrodynamic and stretch effects. This partial stabilization limits further exponential growth. DNS studies confirm that instability amplification tends to saturate at elevated pressures, justifying the transition from an exponential to a quasi-linear scaling [6]. Rather than acting as an empirical tuning constant, this critical pressure threshold is explicitly calculated following the DNS-based scaling methodology, recently validated for engine-like conditions by Scalambro et al. [8]. Specifically, Π_c is formulated as a function of the local equivalence ratio (ϕ) and the normalized unburned gas temperature ($\Theta = T_u / T_{ref}$):

$$\Pi_c = \left(\frac{20\phi}{7 - 2\Theta} \right)^{\frac{150}{21+10\Theta}} \tag{6}$$

By explicitly evaluating Π_c through this closed-form relation, the instability correction naturally saturates as pressure increases during the compression and combustion strokes, avoiding any unphysical divergence. This ensures a completely predictive scaling behavior at high engine loads without requiring any case-by-case calibration of the instability limits. Finally, the resulting instability factor is precomputed over the relevant thermodynamic domain and applied multiplicatively to the laminar flame speed within the 1D combustion framework. It must be noted that, unlike high-fidelity 3D-CFD approaches where local equivalence ratio gradients are explicitly resolved [8], the 0D/1D thermodynamic framework inherently assumes a uniformly mixed unburned zone. Consequently, the instability parameter ω_2 is evaluated using a single, global A/F ratio. While this macroscopic simplification necessarily neglects local stretch–curvature coupling and the spatial stratification of instabilities, it provides an efficient closure to capture the mean-field effect of preferential diffusion on the overall burning velocity.

3.4. NO_X Emissions Modeling

In hydrogen-fueled spark-ignition engines, NO_x represents the primary regulated pollutant, as carbon-based emissions are inherently absent. Under typical engine operating conditions, NO_x formation is dominated by the thermal-NO pathway, which is described by the Extended Zeldovich mechanism [22,23]. The mechanism consists of the following reactions:

$$O + N_2 \leftrightarrow NO + N \tag{7}$$

$$N + O_2 \leftrightarrow NO + O \tag{8}$$

$$N + OH \leftrightarrow NO + H \tag{9}$$

Thermal NO_x formation is generally negligible below approximately 1700 K, while its rate rises sharply as the temperature exceeds 2000 K, and it is strongly dependent on both temperature and oxygen availability. Slightly lean mixtures ($\lambda \approx 1.2$–1.5) typically promote peak NO_x formation due to the combined effect of high combustion temperature and excess oxygen [24].

Within the 0D/1D simulation framework, NO_x formation is evaluated using the global air-to-fuel ratio and the mean burned-gas temperature. Consequently, charge stratification produced by direct injection and the effects of injection timing on the local air–fuel ratio and temperature distributions are not resolved. This simplification remains consistent with the resolution and computational requirements of a system-level model intended for virtual calibration. The reaction rates are expressed in Arrhenius form:

$$k_1 = F_1 \cdot 7.6 \cdot 10^{10} \cdot exp\left(-38000 \cdot \frac{A_1}{T_b}\right) \tag{10}$$

$$k_2 = F_2 \cdot 6.4 \cdot 10^{6} \cdot T_b \cdot exp\left(-3150 \cdot \frac{A_2}{T_b}\right) \tag{11}$$

$$k_3 = F_3 \cdot 4.1 \cdot 10^{10} \tag{12}$$

where T_b is the burned gas temperature; the five parameters F_i and A_i, along with a sixth global multiplier, serve as calibration coefficients. These were optimized using a genetic algorithm to align the kinetic reaction rates and the final predicted NO_x concentrations with the experimental measurements.

Because the burned zone temperature is strongly influenced by instability-enhanced flame propagation, accurate temperature prediction is essential for reliable NO_x estimation. Consequently, the accuracy of the NO_x model is intrinsically coupled to the fidelity of the combustion sub-model.

3.5. Calibration Procedure

A hierarchical calibration methodology was adopted to ensure model robustness and avoid over-parameterization. First, the 0D K-k-ϵ model was tuned against detailed 3D-CFD motoring simulations to provide physically consistent turbulence boundary conditions for the SITurb combustion model. Subsequently, the parameters CTFS, CTLS, and CFKG, introduced in Equations (3) and (4), were optimized using the standard genetic-algorithm procedure recommended in the GT-SUITE User Manual. The objective of the optimization was to minimize the Improved Root Mean Square Error (Improved RMSE) between the predicted and experimentally derived burn-rate profiles, as defined in Equation (13).

$$Burn\ Rate\ Error = \sqrt{\frac{\int_{t_0}^{t_f} \left(LHV_{pred} \cdot BR_{pred} - BR_{meas}\right)^2 dt}{t_f - t_0}} \tag{13}$$

The optimizer was run for a predefined number of iterations using the settings reported in Table 3. At the end of the procedure, the combination of calibration parameters providing the minimum value of the objective function was selected.

Table 3. Parameters of the genetic algorithm used for the combustion model calibration.

Optimization Algorithm	Genetic Algorithm
Objective Function	Improved RMSE on Burn Rate Profile
Population Size	30
Number of Generations	82
Mutation Rate	0.5

The calibration was performed over 12 representative operating points, covering variations in engine speed, load, and relative air–fuel ratio (see Figure 2). In the calibration process, particular attention was given to the flame kernel growth multiplier (CFKG). As recently demonstrated in the literature for ultra-lean hydrogen engines [25], the duration of

the early flame kernel formation is intrinsically and strongly dependent on the equivalence ratio. During this initial phase, the flame radius is smaller than the integral length scale, and its expansion is predominantly governed by spark energy deposition and the mixture's extremely low ignition energy, rather than by the cellular structures induced by thermo-diffusive instabilities. Because the macroscopic entrainment-based SITurb model does not explicitly resolve these micro-scale ignition physics, establishing a λ-dependent functional correlation for CFKG is physically required to accurately capture the mixture-dependent ignition delay (i.e., the early flame development phase). Conversely, the TDI enhancement factor introduced in Section 3.3 specifically governs the fully developed turbulent propagation phase. Therefore, the λ-dependent CFKG does not empirically compensate for a lack of TDI physics; rather, it explicitly and exclusively models the distinct, mixture-dependent kernel development, maintaining strict physical consistency across the operating map. Nevertheless, application of this correlation beyond the investigated λ range may require dedicated recalibration.

In summary, from the combustion perspective, the proposed modeling framework avoids empirical over-fitting by using three distinct sub-models, each dedicated to a specific combustion phase. First, the custom Cantera-derived correlation calculates the laminar flame speed, providing a chemical baseline suited for the high pressures and temperatures of the investigated engine. Second, the λ-dependent CFKG multiplier accounts for the effect of mixture dilution on the initial flame kernel development. Finally, the TDI sub-model governs the main combustion phase, reproducing the flame acceleration typical of ultra-lean hydrogen mixtures. By physically separating these three effects, the framework ensures a consistent prediction of the burn rate across the operating map, explicitly isolating the role of thermo-diffusive instabilities from the baseline chemistry and the early ignition phase.

Finally, as introduced in Section 3.4, the NO_x sub-model multipliers were calibrated across different λ regimes to account for systematic deviations associated with the homogeneous burned-zone assumption. Strict bounds were applied to these calibration ranges to preserve physically realistic activation energies and reaction rate magnitudes. Overall, the calibration strategy successfully balanced physical consistency with high predictive capability across the entire experimental domain.

4. Simulation Results

This section evaluates the predictive capability of the proposed model against the complete experimental database. The analysis proceeds step-by-step to assess the model and explain the underlying physics. First, the specific impact of the TDI correction is quantified through a direct comparison with the baseline formulation. Second, the predictive capabilities of the model, calibrated on the 12 selected operating points, are evaluated across the entire remaining portion of the experimental dataset to assess the accuracy of combustion phasing, burn duration, and peak pressure predictions.

Third, the model's capability to reproduce NO_x emission trends is examined. Finally, a dedicated discussion analyses the physical implications of instability-aware modeling and its relevance for system-level hydrogen engine simulations.

4.1. Impact of Flame Instability Model

To isolate the contribution of the instability-aware formulation, model predictions that include TDI effects are compared against those obtained using the baseline laminar flame speed model without the instability correction (see Figure 3).

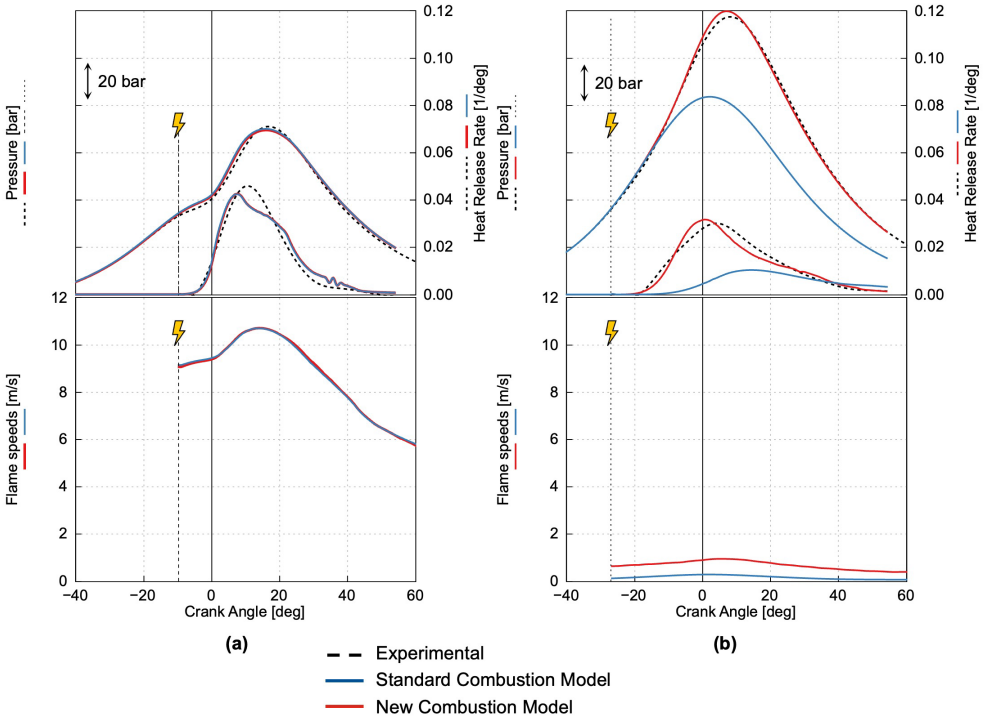


Figure 3. Comparison between experimental (black dashed lines) and predicted in-cylinder pressure and burn rate in the first row. In the second row, predicted flame speeds are reported. Blue: standard combustion model; red: instability-aware model. The yellow markers indicate the spark timing. (**a**): λ = 1.2. (**b**): λ = 3.0 (7500 rpm, 15 bar IMEP-H).

At λ = 1.2 (Figure 3a), both models provide nearly identical predictions of in-cylinder pressure and burn rate. The instability map (Figure 4a) shows that the instability factor S_M/S_L remains close to unity throughout the combustion process, indicating limited thermo-diffusive amplification. Under these conditions, flame propagation is predominantly governed by turbulence–chemistry interactions rather than diffusive-thermal effects. This confirms that the proposed correction does not introduce artificial flame acceleration in regimes where hydrogen–air mixtures are hydrodynamically stable. It is also worth noting that both modeling approaches slightly underestimate the combustion speed between 10 and 20 CAD aTDCf due to the interaction between the modeled flame front and the cylinder liner wall.

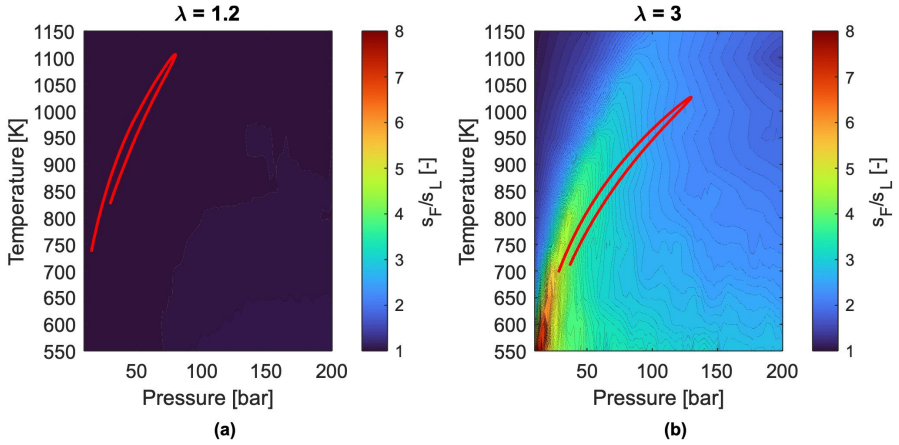


Figure 4. Instability enhancement factor S_M/S_L as a function of in-cylinder pressure and temperature—(**a**): λ = 1.2—(**b**): λ = 3.0. The red line indicates the combustion trajectory.

In contrast, at λ = 3.0 (Figure 3b), the difference between the models becomes substantial. The baseline laminar flame speed model predicts a severely delayed and prolonged combustion process, bordering on misfire-like behavior, which is highly inconsistent with the experimental pressure traces. When TDI effects are included, the predicted burn rate and pressure evolution align closely with the measurements. The instability map (Figure 4b) indicates amplification factors between 3 and 6 along the combustion trajectory, reflecting strong cellular flame development. This demonstrates a systematic discrepancy: neglecting TDI leads to a severe underestimation of the burning velocity in ultra-lean hydrogen mixtures (see Figure 5).

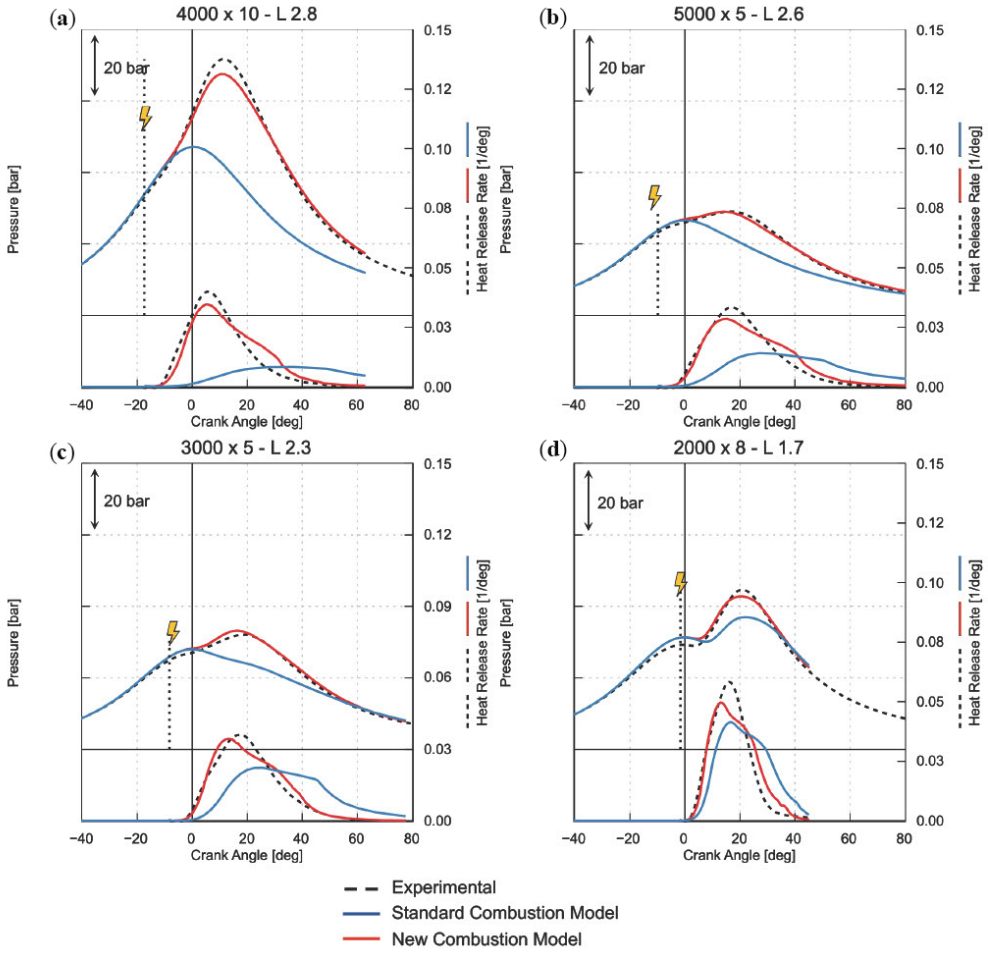


Figure 5. Comparison between experimental and predicted in-cylinder pressure and burn rate in different operating conditions. The yellow markers indicate the spark timing. (**a**): 4000 rpm, 10 bar IMEP-H, λ = 2.8—(**b**): 5000 rpm, 5 bar IMEP-H, λ = 2.6—(**c**): 3000 rpm, 5 bar IMEP-H, λ = 2.3—(**d**): 2000 rpm, 8 bar IMEP-H, λ = 1.7.

Figure 5 provides further evidence of the new model's effectiveness by showing four operating points at low engine speeds and low loads. Due to the highly lean air–fuel ratios, omitting TDI effects causes unacceptable predictive errors even under these milder operating conditions. Furthermore, the slight underestimation of the combustion speed between 10 and 20 CAD aTDCf is clearly visible in these cases, confirming the systematic nature of the interaction between the flame front and the cylinder liner wall.

Finally, Figure 6 summarizes the model's accuracy across the entire experimental dataset by comparing predicted and measured combustion metrics. The instability-aware formulation demonstrates robust predictive capabilities throughout the combustion process. Specifically, the model accurately captures the center of the combustion (see Figure 6a),

predicting the 50% Mass Fraction Burned (MFB50) within a narrow margin of ±3 CAD for the vast majority of the operating points. Similarly, the overall combustion duration (see Figure 6b), represented by the MFB10–75 interval, is reproduced with an error bounded within 5 CAD, indicating a highly reliable description of the heat release profile. This precision in tracking the combustion phasing naturally translates into accurate in-cylinder pressure predictions: average deviations for the peak pressure magnitude (see Figure 6c) are limited to approximately 5 bar, while the corresponding crank angle timing (see Figure 6d) is predicted with an error of less than 5 CAD. By contrast, the baseline model exhibits a systematic and growing predictive error as the mixture becomes leaner. This diverging trend definitively confirms that thermo-diffusive instability effects are not merely marginal, but become the governing mechanism in ultra-lean hydrogen operation.

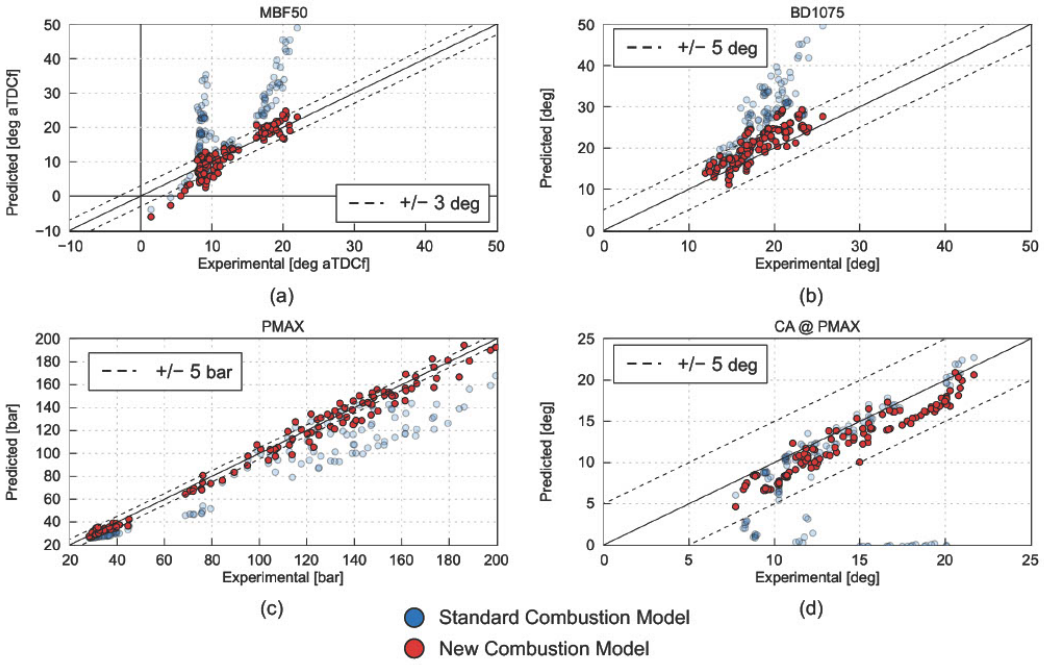


Figure 6. Correlation between experimental and predicted combustion metrics: (**a**): MFB50—(**b**): MFB10–75—(**c**): peak pressure—(**d**): crank angle at peak pressure. Blue: baseline model; red: instability-aware model.

4.2. Sensitivity Analysis

Beyond the pointwise correlation, the robustness of the model is evaluated through controlled variations in engine air–fuel ratio (see Figure 7b), load (see Figure 7c), and speed (see Figure 7d) starting from a baseline condition at 6000 rpm, 17 bar IMEP-H, and $\lambda = 1.35$ (see Figure 7a). When the engine speed is increased to 7500 rpm, the model accurately captures the expected acceleration of combustion driven by the increased turbulence intensity. Similarly, when the load is raised to 26 bar IMEP-H, the predicted rise in peak pressure and heat release rate magnitude is highly consistent with the experimental trends. Furthermore, under highly lean operation ($\lambda = 2.5$), the model correctly reproduces the expected increase in combustion duration and the reduction in heat release magnitude, while strictly maintaining accurate combustion phasing. These results indicate that the instability-aware framework does not compromise the model's sensitivity to turbulence or to varying thermodynamic boundary conditions.

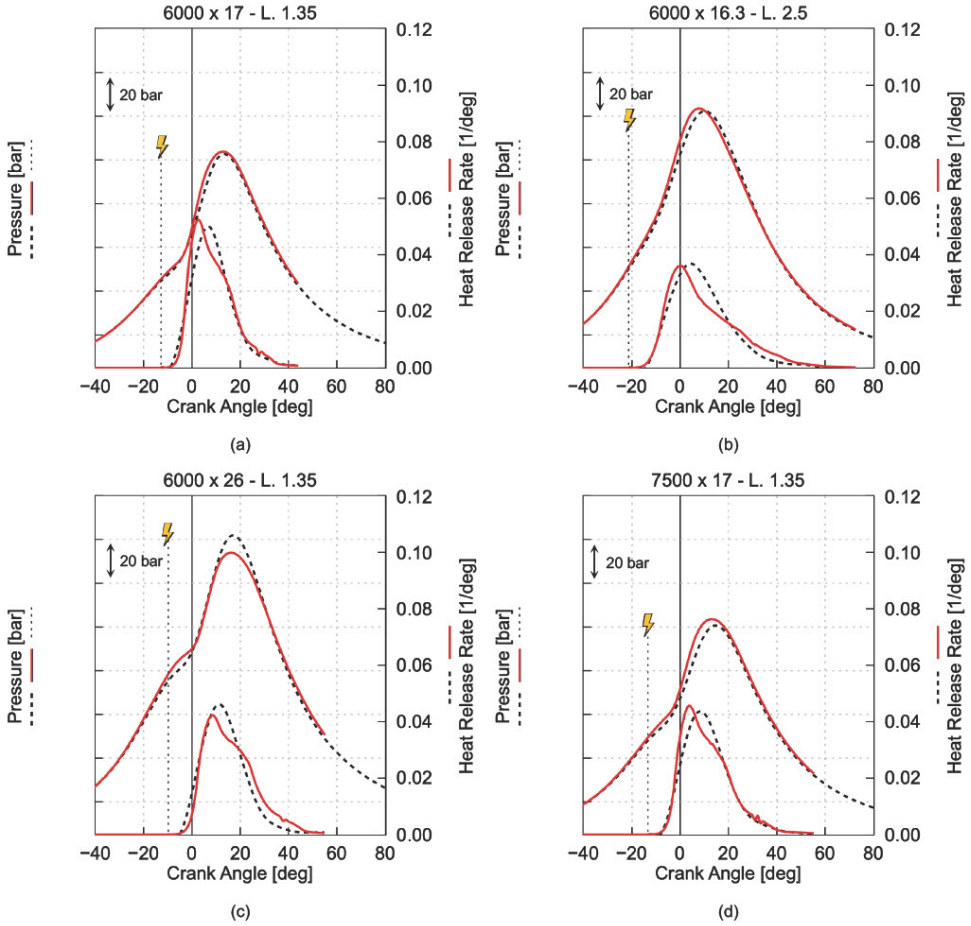


Figure 7. Model sensitivity to operating conditions. The yellow markers indicate the spark timing. (**a**): baseline: 6000 rpm, 17 bar IMEP-H, λ = 1.35—(**b**): effect of λ: 6000 rpm, 16.3 bar IMEP-H, λ = 2.50—(**c**): effect of load: 6000 rpm, 26 bar IMEP-H, λ = 1.35—(**d**): effect of speed: 7500 rpm, 17 bar IMEP-H, λ = 1.35.

4.3. NO_x Emission Model

Figure 8 presents the correlation between the predicted and measured NO_x concentrations. While the Extended Zeldovich mechanism relies on multipliers tuned over a restricted calibration subset, the model is able to effectively generalize across a broader validation dataset, achieving an overall average error of approximately 20%. This confirms that the calibrated sub-model provides reliable predictions consistent with state-of-the-art 1D simulation approaches [26,27].

Furthermore, Figure 9 illustrates a λ sweep at a fixed speed and load of 6000 rpm and 15 bar IMEP-H. The model successfully reproduces the characteristic bell-shaped NO_x trend, with peak emissions occurring between λ = 1.0 and 1.5, followed by a strong reduction in the ultra-lean regimes (λ > 2.0). Under near-stoichiometric conditions, the model slightly underestimates the peak NO_x with an absolute error of approximately 1000 ppm. This underprediction may be related to charge stratification generated by the injection strategy. Injection timing affects the time available for fuel–air mixing and, consequently, the local air–fuel ratio and temperature distributions within the combustion chamber. These spatial effects cannot be captured by the present 0D/1D formulation, which uses a global air-to-fuel ratio. This simplified approach was retained to preserve the low computational cost required for virtual calibration over a wide operating map. Nevertheless, the model correctly reproduces the global NO_x trend and order of magnitude, with an overall accuracy in line with comparable 0D/1D modeling approaches reported in the literature.

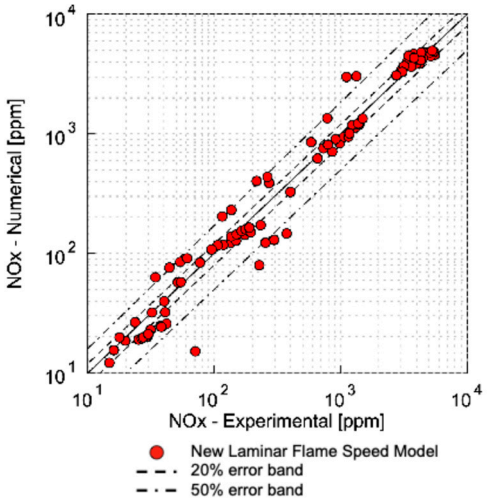


Figure 8. Experimental vs. predicted NO_x concentrations with 20% and 50% error bands.

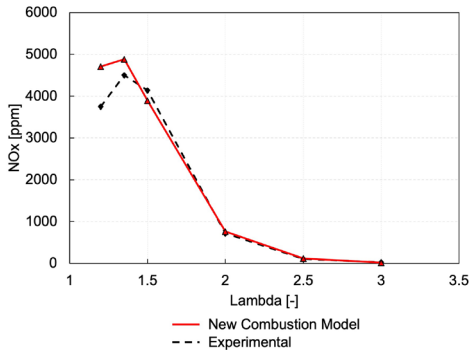


Figure 9. NO_x emissions versus λ at 6000 rpm and 15 bar IMEP-H. Experimental (black dashed) and predicted (red).

To further evaluate the model's predictive capability under part-load conditions—which are highly relevant for real-world driving scenarios—Figure 10 illustrates the emission trends for two load sweeps performed at 2000 rpm (Figure 10a) and 3000 rpm (Figure 10b).

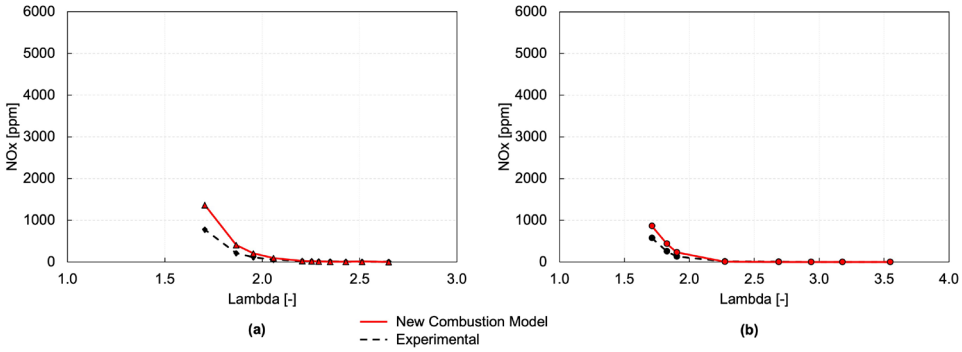


Figure 10. NO_x Emission Variation versus Load and λ. (**a**): Load Sweep 5–7.5 bar IMEP-H at 2000 RPM. (**b**): Load Sweep 3.7–7 bar IMEP-H at 3000 RPM.

In these test sequences, the engine load is varied with the progressive reduction in the relative air–fuel ratio. While these do not represent constant-load λ sweeps, they accurately reflect typical engine operating conditions. As observed in Figure 10, the model satisfactorily tracks the sharp, exponential increase in NO_x emissions as λ is reduced from ultra-lean conditions ($\lambda > 2.0$) toward richer mixtures ($\lambda \approx 1.7$). Although the model slightly overpredicts the absolute NO_x magnitude at the lowest λ values of these sweeps, it correctly

reproduces the global trend and the critical transition region where thermal NO_x formation becomes rapidly significant.

5. Discussion

The results highlight that thermo-diffusive instability is not a secondary correction, but a governing mechanism in ultra-lean hydrogen combustion. While entrainment-based turbulent models adequately describe flame propagation under near-stoichiometric conditions, they become systematically inaccurate when preferential diffusion effects dominate the evolution of the flame structure.

From a modeling perspective, two key aspects emerge. First, the instability correction primarily acts on the laminar flame speed term. In the SITurb formulation, this term directly influences both the entrainment rate and the burn-up time scale. Consequently, even a moderate underprediction of the laminar flame speed propagates nonlinearly into combustion phasing and duration errors. This explains the nonlinear increase in predictive deviation observed at higher λ values when TDI effects are neglected (as seen in Figure 6). Second, the pressure-dependent transition between exponential and quasi-linear instability amplification reflects the competition between diffusive enhancement and pressure-induced stabilization. As the in-cylinder pressure increases during combustion, the flame thickness decreases, and transport-driven cellular growth becomes progressively constrained. Adopting a bounded instability scaling is therefore necessary to ensure physical consistency during high-load operation.

These findings align with high-fidelity investigations of lean hydrogen flames [6] and recent engine-relevant instability analyses [8], which emphasize the dominant role of preferential diffusion under lean conditions. However, the current work extends these insights to system-level simulations, proving that instability-aware closures are essential to maintain predictive accuracy across complete engine operating maps.

It should be acknowledged that the 0D/1D framework assumes spatial homogeneity within the burned and unburned zones. Therefore, it does not explicitly resolve local stratification, stretch–curvature coupling, or small-scale turbulence–instability interactions. The instability correction introduced here is an effective macroscopic modeling approach rather than a detailed microscopic description of flame cellularity. Nonetheless, the strong agreement with the experimental data confirms that the dominant macroscopic effects are captured with the accuracy required for calibration-oriented simulations.

Overall, neglecting thermo-diffusive effects in hydrogen engine modeling introduces a structural bias under lean operation. Conversely, instability-aware formulations offer a physically consistent pathway to extend predictive capabilities toward ultra-lean and high-speed regimes. Beyond combustion phasing, thermo-diffusive instability also indirectly affects NO_x formation by influencing the evolution of the burned gas temperature. By accelerating flame propagation under ultra-lean conditions, the instability-aware model modifies both the peak temperature and the residence time within high-temperature zones, which are the primary drivers of thermal NO_x production. The satisfactory agreement observed in the global NO_x correlation (Figure 8) and the λ-sweep analyses (Figures 9 and 10) further supports the internal consistency of this coupled combustion-emission framework. Although the Extended Zeldovich mechanism is a simplified representation of nitrogen chemistry, these results demonstrate that accurately modeling instability-enhanced flame propagation is a fundamental prerequisite for reliable system-level emission predictions in lean hydrogen engines.

6. Conclusions

This study presented the development and validation of an instability-aware 0D/1D combustion model for a high-performance, direct injection hydrogen spark-ignition engine. The framework combines an entrainment-based turbulent combustion model with a custom laminar flame speed correlation derived from detailed chemical kinetics. Crucially, it integrates a thermo-diffusive instability correction based on linear flame stability theory and DNS-informed scaling.

The results demonstrate that thermo-diffusive instability is a governing mechanism in ultra-lean hydrogen operation, not merely a marginal effect. When these instability effects are neglected, conventional system-level models systematically underestimate the burning velocity, leading to growing errors in combustion phasing and duration as mixture dilution increases. Incorporating the instability-aware correction successfully restores predictive consistency across the entire operating domain (2000–7500 rpm, up to 28 bar IMEP-H, and λ = 1.2–3.0). The model predicts combustion phasing within $\pm$3 CAD and NO_x emissions with an average deviation of approximately 20%.

Beyond numerical accuracy, the primary contribution of this work is establishing a physically consistent method to embed thermo-diffusive instability effects into computationally efficient engine models. This approach extends 1D-CFD predictive capabilities into ultra-lean, high-speed regimes without relying on purely empirical corrections. While the current formulation assumes homogeneous burned and unburned zones—and thus does not resolve local stratification or microscopic turbulence–instability interactions—the strong agreement with experimental data confirms that the dominant macroscopic impacts of preferential diffusion are effectively captured. Future developments will focus on embedding the effects of charge and thermal stratification within the thermodynamic framework. By explicitly accounting for the local mixture distribution, this enhancement will allow for a more localized evaluation of the ω_2 parameter—further aligning the system-level approach with 3D-CFD evidence [8]—and concurrently refine the accuracy of the highly nonlinear nitrogen chemistry for NO_x prediction, without compromising the overall computational efficiency. Furthermore, since the present conclusions are derived from a single-cylinder research engine equipped with resonators to emulate multicylinder gas dynamics, additional investigations will be carried out to extend the validation of this combustion model to a complete multicylinder architecture.

Moreover, future developments will include an explicit dependence on the EGR level, since its absence represents a significant limitation of the current model. The laminar flame speed correlation will first be extended through additional 1D Cantera simulations including EGR dilution, and then, if necessary, the combustion model calibration coefficients will be re-optimized, focusing mainly on the dilution-effect multiplier. The updated model will be validated using data from the ongoing experimental campaign at different external EGR levels.

Ultimately, this framework provides a robust foundation for the virtual calibration and parametric optimization of highly diluted hydrogen engines. It represents a practical tool for industrial workflows, contributing to the development of high-efficiency, high-specific-power hydrogen powertrains.

Author Contributions: Conceptualization, L.R., A.P., and G.M.; Methodology, L.R., A.P., G.M., and F.M. (Fabio Mortellaro); Validation, G.M.; Formal Analysis, G.M.; Writing—original draft preparation, G.M.; Writing—review and editing, L.R., A.P., and F.M. (Federico Millo); Supervision, L.R., A.P., and F.M. (Federico Millo), R.T. All authors have read and agreed to the published version of the manuscript.

Funding: This research received no external funding.

Data Availability Statement: The data supporting the findings of this study cannot be shared because they are commercially sensitive and subject to a confidentiality agreement with the industrial partner.

Conflicts of Interest: Authors Fabio Mortellaro and Roberto Tonelli are employed by the company Ferrari Spa. The remaining authors declare that the research was conducted in the absence of any commercial or financial relationships that could be construed as a potential conflict of interest.

Abbreviations

The following abbreviations are used in this manuscript:

1D-CFD	One-Dimensional Computational Fluid Dynamics
3D-CFD	Three-Dimensional Computational Fluid Dynamics
aTDCf	After Top Dead Center firing
bTDCf	Before Top Dead Center firing
BR	Burn Rate
CAD	Crank Angle Degrees
CFKG	Flame Kernel Growth multiplier coefficient
CoC	Center of Combustion
DI	Direct Injection
DNS	Direct Numerical Simulations
EZM	Extended Zeldovich Mechanism
GDI	Gasoline Direct Injection
H_2-ICE	Hydrogen Internal Combustion Engine
HFM	Hot Film Anemometer
HRR	Heat Release Rate
ICE	Internal Combustion Engine
IMEP	Indicated Mean Effective Pressure
IMEP-H	Indicated Mean Effective Pressure-Gross
LFS	Laminar Flame Speed
MBT	Maximum Brake Torque
MFB	Mass Fraction Burned
NO_x	Nitrogen Oxides
RMSE	Root Mean Squared Error
SCE	Single-Cylinder Engine
SI	Spark Ignition
SITurb	Spark-Ignition Turbulent
SOI	Start of Injection
TDI	Thermo-Diffusive Instability
TKE	Turbulent Kinetic Energy
VVT	Variable Valve Timing

References

1. Sterlepper, S.; Fischer, M.; Claßen, J.; Huth, V.; Pischinger, S. Concepts for Hydrogen Internal Combustion Engines and Their Implications on the Exhaust Gas Aftertreatment System. *Energies* **2021**, *14*, 8166. [CrossRef]
2. Verhelst, S. Recent Progress in the Use of Hydrogen as a Fuel for Internal Combustion Engines. *Int. J. Hydrogen Energy* **2014**, *39*, 1071–1085. [CrossRef]
3. Yip, H.L.; Srna, A.; Yuen, A.C.Y.; Kook, S.; Taylor, R.A.; Yeoh, G.H.; Medwell, P.R.; Chan, Q.N. A Review of Hydrogen Direct Injection for Internal Combustion Engines: Towards Carbon-Free Combustion. *Appl. Sci.* **2019**, *9*, 4842. [CrossRef]
4. Eicheldinger, S.; Waligorski, D.; Wachtmeister, G.; Jaensch, M. Performance Potential of Hydrogen Combustion Engines for Industrial Applications. *MTZ Worldw.* **2022**, *83*, 60–64. [CrossRef]
5. Howarth, T.L.; Aspden, A.J. An Empirical Characteristic Scaling Model for Freely-Propagating Lean Premixed Hydrogen Flames. *Combust. Flame* **2022**, *237*, 111805. [CrossRef]
6. Howarth, T.L.; Hunt, E.F.; Aspden, A.J. Thermodiffusively-Unstable Lean Premixed Hydrogen Flames: Phenomenology, Empirical Modelling, and Thermal Leading Points. *Combust. Flame* **2023**, *253*, 112811. [CrossRef]

7. Gomez-Soriano, J.; Sapkota, P.; Wijeyakulasuriya, S.; D'Elia, M.; Probst, D.; Viswanathan, V.; Olcina-Girona, M.; Novella, R. Numerical Modeling of Hydrogen Combustion Using Preferential Species Diffusion, Detailed Chemistry and Adaptive Mesh Refinement in Internal Combustion Engines. In Proceedings of the 16th International Conference on Engines & Vehicles, Capri, Italy, 10–14 September 2023.
8. Scalambro, A.; Piano, A.; Millo, F. Modelling Thermodiffusive Instabilities in Hydrogen Flames and Their Impact on the Combustion Process in a Direct-Injection Hydrogen Engine. *Combust. Flame* **2025**, *282*, 114457. [CrossRef]
9. Blizard, N.C.; Keck, J.C. Experimental and Theoretical Investigation of Turbulent Burning Model for Internal Combustion Engines. In Proceedings of the 1974 Automotive Engineering Congress and Exposition, Detroit, MI, USA, 25 February–1 March 1974.
10. Morel, T.; Rackmil, C.I.; Keribar, R.; Jennings, M.J. Model for Heat Transfer and Combustion in Spark Ignited Engines and Its Comparison with Experiments. In Proceedings of the SAE International Congress and Exposition, Detroit, MI, USA, 29 February–4 March 1988.
11. De Bellis, V.; Piras, M.; Bozza, F.; Malfi, E.; Novella, R.; Gomez-Soriano, J.; Olcina-Girona, M. Development and Validation of a Phenomenological Model for Hydrogen Fueled PFI Internal Combustion Engines Considering Thermo-Diffusive Effects on Flame Speed Propagation. *Energy Convers. Manag.* **2024**, *308*, 118395. [CrossRef]
12. Landau, L. On the Theory of Slow Combustion. In *Dynamics of Curved Fronts*; Academic Press: Boston, MA, USA, 1988; pp. 403–411.
13. Matalon, M.; Cui, C.; Bechtold, J.K. Hydrodynamic Theory of Premixed Flames: Effects of Stoichiometry, Variable Transport Coefficients and Arbitrary Reaction Orders. *J. Fluid Mech.* **2003**, *487*, 179–210. [CrossRef]
14. Medda, M.; Calia, V.; Di Sacco, M.; Gullino, F.; Rossi, V.; Silvestri, N.; Tonelli, R.; Zaffino, F. Challenges and Opportunities in Developing a Hydrogen High Specific Power SCE in the Roadmap towards Zero Net GHG. In Proceedings of the 32nd Aachen Colloquium, Aachen, Germany, 9–11 October 2023.
15. Bosch Gmbh. Bosch Sensor Catalog. Available online: https://www.bosch-ibusiness.com/media/downloads/kataloge/sensoren/2026_03_sensors_i-business.pdf (accessed on 1 March 2026).
16. Fogla, N.; Bybee, M.; Mirzaeian, M.; Millo, F.; Wahiduzzaman, S. Development of a K-k-ϵ Phenomenological Model to Predict in-Cylinder Turbulence. *SAE Int. J. Engines* **2017**, *10*, 562–575. [CrossRef]
17. Kéromnès, A.; Metcalfe, W.K.; Heufer, K.A.; Donohoe, N.; Das, A.K.; Sung, C.-J.; Herzler, J.; Naumann, C.; Griebel, P.; Mathieu, O.; et al. An Experimental and Detailed Chemical Kinetic Modeling Study of Hydrogen and Syngas Mixture Oxidation at Elevated Pressures. *Combust. Flame* **2013**, *160*, 995–1011. [CrossRef]
18. Sapio, F.; Aglietti, F.; Ferreri, P.; Savuca, A. Neural-Network-Based Modeling of SCR Systems for Emission Simulation: A Comprehensive Approach. *SAE Int. J. Adv. Curr. Pract. Mobil.* **2024**, *7*, 1437–1452. [CrossRef]
19. Goodwin, D.G.; Speth, R.L.; Moffat, H.K.; Weber, B.W. *Cantera: An Object-Oriented Software Toolkit for Chemical Kinetics, Thermodynamics, and Transport Processes*; Zenodo: Geneva, Switzerland, 2022.
20. Konnov, A.A. Yet Another Kinetic Mechanism for Hydrogen Combustion. *Combust. Flame* **2019**, *203*, 14–22. [CrossRef]
21. Liu, X.; Menaca, R.; Mortellaro, F.S.; Medda, M.; Zou, J.; Farooq, A.; Im, H.G. Evaluation of Chemical Kinetic Mechanisms for Hydrogen Engine Modeling. *Chem. Eng. J.* **2025**, *524*, 169082. [CrossRef]
22. Zeldovich, J. The Oxidation of Nitrogen in Combustion and Explosions*. *Eur. Phys. J. A Hadrons Nucl.* **1946**, *21*, 577–628.
23. Liberman, M.A. *Introduction to Physics and Chemistry of Combustion*; Springer: Berlin/Heidelberg, Germany, 2008.
24. Sher, E. *Handbook of Air Pollution from Internal Combustion Engines Pollutant Formation and Control*; Academic Press: Boston, MA, USA, 1998.
25. Bozza, F.; De Bellis, V.; Teodosio, L.; Pretto, M.; Giannattasio, P.; Novella, R.; Gomez-Soriano, J. Impact of Flame Kernel Formation Process on Ultra-Lean Hydrogen Combustion in Spark-Ignition Engines: Modeling and Experimental Validation. *Appl. Therm. Eng.* **2026**, *291*, 130203. [CrossRef]
26. Özgül, E.; Bedir, H. Fast NO_x Emission Prediction Methodology via One-Dimensional Engine Performance Tools in Heavy-Duty Engines. *Adv. Mech. Eng.* **2019**, *11*, 1687814019845954. [CrossRef]
27. Esposito, S.; Diekhoff, L.; Pischinger, S. Prediction of Gaseous Pollutant Emissions from a Spark-Ignition Direct-Injection Engine with Gas-Exchange Simulation. *Int. J. Engine Res.* **2021**, *22*, 3533–3547. [CrossRef]

Disclaimer/Publisher's Note: The statements, opinions and data contained in all publications are solely those of the individual author(s) and contributor(s) and not of MDPI and/or the editor(s). MDPI and/or the editor(s) disclaim responsibility for any injury to people or property resulting from any ideas, methods, instructions or products referred to in the content.